This is an *Accepted Manuscript*, which has been through the Royal Society of Chemistry peer review process and has been accepted for publication.

Accepted Manuscripts are published online shortly after acceptance, before technical editing, formatting and proof reading. Using this free service, authors can make their results available to the community, in citable form, before we publish the edited article. We will replace this *Accepted Manuscript* with the edited and formatted *Advance Article* as soon as it is available.

You can find more information about *Accepted Manuscripts* in the **Information for Authors**.

Please note that technical editing may introduce minor changes to the text and/or graphics, which may alter content. The journal's standard **Terms & Conditions** and the **Ethical guidelines** still apply. In no event shall the Royal Society of Chemistry be held responsible for any errors or omissions in this *Accepted Manuscript* or any consequences arising from the use of any information it contains.

Theoretical study on the injection, transport, absorption and phosphorescence properties of heteroleptic iridium(III) complexes with different ancillary ligands

Xiaohong Shang, [a] Ning Wan,[b] Deming Han,*[c] and Gang Zhang[d]

[a] College of Chemistry and Life Science, Changchun University of Technology, Changchun 130012, P.R. China. E-mail:shangxiaohong58@aliyun.com
[b] Computer Information Network Center, Changchun University of Technology, Changchun 130012, P.R. China
[c] School of Life Science and Technology, Changchun University of Science and Technology, Changchun 130022, P.R. China
[d] State Key Laboratory of Theoretical and Computational Chemistry, Institute of Theoretical Chemistry, Jilin University, Changchun 130023, P.R. China

We have reported a theoretical analysis of a series of heteroleptic iridium(III) complexes (mpmi)$_2$Ir(fppi) [mpmi = 1-(4-tolyl)-3-methyl-imidazole, fppi = 4-fluoro-2-(pyrrol-2-yl)-pyridine] (**1a**), (mpmi)$_2$Ir(dfpi) [dfpi = 4-fluoro-2-(3-fluoro-pyrrol-2-yl)-pyridine] (**1b**), (mpmi)$_2$Ir(tfpi) [tfpi = 2-(pyrrol-2-yl)-4-trifluoromethyl-pyridine] (**1c**), (mpmi)$_2$Ir(priq) [priq = 1-(pyrrol-2-yl)isoquinoline] (**2a**), (mpmi)$_2$Ir(isql) [isql = 1-(indol-2-yl)-isoquinoline] (**2b**), and (mpmi)$_2$Ir(biql) [biql = 1-(benzoimidazol-2-yl)-isoquinoline] (**2c**) by using the density functional theory (DFT) method to investigate their electronic structures, photophysical properties, and the phosphorescent efficiency mechanism. The results reveal that the nature of the ancillary ligands can affect the electron density distributions and energies of frontier molecular orbitals, resulting in the changes of charge transfer performances and emission color. It is found that the studied complex

1c with the -CF$_3$ substituent at the pyridine moiety renders the lower HOMO-LUMO energy gap and LUMO energy level, which will lead to a rich electron injection ability compared with that of **1a**. For each complexes studied (except **2b**), the hole-transporting performance is better than the electron-transporting performance. In addition, for complex **2a** and **2b**, the difference between reorganization energies for hole transport (λ_{ih}) and reorganization energies for electron transport (λ_{ie}) are relatively smaller, indicating that the hole and electron transfer balance could be achieved more easily in the emitting layer. It is believed that the largest metal to ligand charge transfer (MLCT) character, the higher μ_{S_1} and E_{T_1} values, as well as the smallest $\Delta E_{S_1 - T_1}$ value could result in the larger phosphorescent quantum efficiency for **1b** than those of other complexes.

Introduction

Phosphorescent metal complexes have become the research core in the field of optoelectronic materials since the Pt-porphyrin complexes have been successfully applied in organic light emitting diodes (OLEDs) in 1998.[1] Phosphorescent materials based on heavy transition-metal complexes, such as Os(II), Pt(II), Ru(II), Re(I), and Ir(III), have received intensive attention due to their potential application as highly efficient electron luminescent emitters in OLEDs.[2–5] Due to the heavy atom induced spin-orbit coupling (SOC) effect, which can partially remove the spin-forbidden nature of the T$_1$→S$_0$ radiative relaxation, the electrophosphorescence can make use of both singlet and triplet excitons and achieve a theoretical level of unity for the internal quantum efficiency, rather than the 25% inherent upper limit imposed by the formation of singlet excitons for the respective fluorescent materials.[6,7] Among third-row transition metals, iridium(III)-based complexes are particularly promising candidates because of their high emission efficiency, short triplet radiative lifetimes, good thermal stability, and wide range of emission colors compared with the other metal complexes.[8–10]

For the realization of full-color displays, many interesting iridium(III) complexes

emitting in green (such as Ir(ppy)$_3$ and Ir(dfppy)$_2$(acac), ppy = 2-phenylpyridine, dfppy = 4,6-difluoro-phenylpyridine, acac = acetylacetonate), red (such as Ir(piq)$_3$, piq = 1-phenylisoquinolato), blue (such as, Ir(dfppy)$_2$(pic), pic = picolate), and other color regions have been developed with good device performances.[11–17] Recently, Chen et al. reported a series of bis(carbene) cyclometalated Ir(III) complexes with N,N-heteroaromatic as ancillary ligands, indicating the possibility of altering the emission color over a wide range, which have also been successfully used in the electroluminescence devices with extremely high device efficiencies. Through the synthesized complex (mpmi)$_2$Ir(priq),[18] where mpmi = 1-(4-tolyl)-3-methyl-imidazole, priq = 1-(pyrrol-2-yl)isoquinoline (**2a**) in Fig. 1, a series of phosphorescent iridium(III) complexes (**1a**, **1b**, **1c**, **2b**, and **2c**) have been theoretically designed, that is, (mpmi)$_2$Ir(fppi) [fppi = 4-fluoro-2-(pyrrol-2-yl)-pyridine] (**1a**), (mpmi)$_2$Ir(dfpi) [dfpi = 4-fluoro-2-(3-fluoro-pyrrol-2-yl)-pyridine] (**1b**), (mpmi)$_2$Ir(tfpi) [tfpi = 2-(pyrrol-2-yl)-4-trifluoromethyl-pyridine] (**1c**), (mpmi)$_2$Ir(isql) [isql = 1-(indol-2-yl)-isoquinoline] (**2b**), and (mpmi)$_2$Ir(biql) [biql = 1-(benzoimidazol-2-yl)-isoquinoline] (**2c**) with the ligand of 1-(4-tolyl)-3-methyl-imidazole. In our present work, the main goal is to theoretically provide a detailed understanding of physical properties, such as the electronic structures, charge injection and transport, and spectral properties.

Computational details

The ground state and the lowest lying triplet excited state geometries were carried out using the density functional theory (DFT)[19] with Becke's three parameter hybrid method[20] combined with the Lee-Yang-Parr correlation functional[21] (denoted as B3LYP). Restricted and unrestricted[22] formalisms were adopted in the singlet and triplet geometry optimization, respectively. All geometrical structures were fully optimized without any symmetry constraints. Vibrational frequencies were also calculated at the same theoretical level, which confirms that each configuration was

a minimum on the potential energy surface. In order to choose the suitable calculation method, hybrid Hartree-Fock/density functional model (PBE0) based on the Perdew-Burke-Erzenrhof (PBE)[23] is also applied. The basis set effect has been tested using different combinations of basis sets for metal and main group atoms. The quasi-relativistic pseudopotentials of Ir atoms proposed by Hay and Wadt with 17 valence electrons were employed, and a ''double-ξ'' quality basis set LANL2DZ was adopted as the basis set.[24] For other atoms, 6-31G(d), 6-31+G(d), and 6-311+G(d) basis sets were employed. On the basis of the optimized ground- and lowest excited-state equilibrium geometries, the time-dependent density functional theory (TDDFT)[25] approach associated with the polarized continuum model (PCM)[26] in dichloromethane (CH_2Cl_2) medium was applied to investigate the absorption and emission spectral properties from the experimental results by Chen et al.[18] Moreover, to find a reliable method to predict the emission properties, five different density functionals (B3LYP, M062X,[27] PBE1PBE (also called PBE0), BP86,[28] and CAM-B3LYP[29]) were performed to calculate the emission spectra for **2a**. It can be found that the M062X functional gave the more satisfactory emission properties for these Ir(III) complexes. All calculations were performed with the B.01 revision of the Gaussian 09 program package,[30] the GaussSum 2.5 program[31] being used for the UV/vis absorption spectral analysis.

Results and discussion

Computational methods and basis sets

In order to propose a suitable method for theoretical calculations of Ir(III) complexes studied here, the structure parameters of complex **2a** have been computed with PBE0 and B3LYP methods using different basis sets and were compared with the experimental results (X-ray crystal structure data) (see Table S1 (Supplementary Information) for details).[18] Fig. 2 showed the variations of calculated bond lengths compared with the experimental results for complex **2a**. Herein, the Ir-related bond lengths in complex **2a** were paid special attention in the geometry optimization. To

check the computational method, two different density functionals (B3LYP and PBE0) were used. A good agreement with experimental data was obtained for DFT/PBE0 method with 6-31G(d), 6-31+G(d), and 6-311+G(d) basis sets, even though it overestimates Ir-N2 bond lengths with variation more than 0.03 Å, while a disagreement was found for B3LYP method, especially the bond lengths of Ir-N2 with the deviation more than 0.08 Å. Hence, PBE0 is a better method to give theoretical insights into this kind of compounds. Because there is not great basis set effect on the structural parameters, the calculated data by the basis set of 6-31G(d) are good enough to predict the structures and properties of the complexes.

Molecular geometries in the ground and lowest triplet states

The representative optimized structure of **2a** in the ground state (S_0) at PBE0 level are shown in Fig. 3 along with the numbering of some key atoms. The main optimized geometry parameters for these complexes in ground state (S_0) and lowest lying triplet excited state (T_1) are summarized in Table 1. The dihedral angles of N1-Ir-N2-C1 and C1-Ir-C2-C3 are about 90º, indicating the perpendicular of three ligands.

The introduction of different substituents on the ancillary ligands ($N^\wedge N$) has the large effect on geometrical parameters for **1a-1c**. The Ir-N1 and Ir-N2 bond distances are obviously elongated in **1b** (2.132 Å, 2.180 Å) and **1c** (2.127 Å, 2.176 Å) compared with **1a** (2.122 Å, 2.169 Å). Table 1 also shows that the change of the $N^\wedge N$ ligands for complexes **2a-2c** has a significant influence on the metal-ligand bond distances, which is probably due to the large π-conjugated extension and the large steric hindrance in the $N^\wedge$isoquinoline type ligand in **2a-2c** than the $N^\wedge$pyridine type ligand in **1a-1c**. For **2a-2c**, metal-ligand bond distances can be affected by the competition between π-conjugated extension and steric hindrance. Especially, the bond distances of Ir-N1 and Ir-N2 in **2a** are significantly shortened. This indicates the strong interaction between the Ir(III) center and the $N^\wedge N$ ligand, which may also increase the probability of charge transfer from metal to $N^\wedge N$ ligand in **2a**.

In order to demonstrate the changes of geometry parameters upon excited, the

geometry parameters of **1a-2c** in the triplet excited states (T_1) were also calculated. The changes of the selected Ir(III)-related bond lengths from ground to excited state for all complexes are shown in Fig. 4 and Table 1. For the T_1 state, the bond distances of Ir-N2 for all these complexes are significantly shorter than those in the S_0 state. Fig. 4 shows that **1c** have the largest changes of bond distances between S_0 and T_1 states, which can increase the interaction of metal-N$^\wedge$N ligand and might consequently result in the decrease of metal-centered (MC) nonradiative emission and enhancement of radiative deactivation compared with other complexes. In addition, the Ir-C (Ir-C1, Ir-C2, and Ir-C3) bond were slightly changes with respect to those of S_0 state. The change indicates that in T_1 state, the interaction between metal and N$^\wedge$N ligand is strengthened, whereas the interaction between metal and the cyclometalated ligands are weakened. Furthermore, this different interaction strength between the metal and the cyclometalated ligands or N$^\wedge$N ligand will result in different electronic transition characters.

Frontier molecular orbitals analysis

It is well known that the optical and chemical properties of these complexes are mainly dependent on the changes of the ground state electronic structures. Herein, we will discuss in detail the ground state electronic structures of these complexes by focusing on the frontier molecular orbitals (FMOs) components and energy levels. The contour plots of the calculated energy of the highest occupied molecular orbital (HOMO), lowest unoccupied molecular orbital (LUMO), and the HOMO-LUMO energy gaps of these studied complexes are plotted in Fig. 5. The detailed descriptions of the molecular orbitals, % composition of ligands and metal orbitals, and the assignment of different fragments at the PBE0/6-31G(d) level are collected in Tables S2-S7 (Supplementary Information).

For **1a**, the electron density in the HOMO is predominantly delocalized over N$^\wedge$N part (73%) extending to the Ir atom and C$^\wedge$C moiety with a small proportion (about 13%). The calculated results reveal that introduction of F substitution in R_2 position in **1b** and the substitution of the F group by the -CF$_3$ group on the R_1

positionin **1c** (Fig. 1) leads to a significant influence on compositions of related FMOs compared with that of **1a**. For **1b** and **1c**, a contribution of 37% and 21% from the metal 5d orbitals, respectively, are responsible for the HOMO distribution. In addition, the HOMO in **1b** is composed of the C$^\wedge$C moiety (50%) and the N$^\wedge$N moiety (13%). The HOMO in **1c** is mainly based on the N$^\wedge$N (54%) moiety, along with 25% of the C$^\wedge$C moiety contribution.

Owing to the change of the ancillary ligands, the HOMO of **2a** and **2b** are mainly based on the N$^\wedge$N (73% and 83%, respectively), while in **2c**, the 32% metal 5d orbital and 31% π(C$^\wedge$C) are responsible for the HOMO together with the non-negligible distribution localized on ancillary ligand (N$^\wedge$N) (37%). On the other hand, the introduction of the CF$_3$ substituent at R$_1$ position of the pyridine moiety in N$^\wedge$N ligand (**1c**) and change of the ancillary ligands (**2a-2c**) has a significant effect on the FMO energy levels as shown in Fig. 5. For **1c** and **2a-2c**, stabilizes the LUMO energy levels more markedly than that of the HOMO, which results in a decrease of the HOMO-LUMO energy gap in comparison with that of **1a** and **1b**, while the changes predicted on the LUMO energy levels seem inevitable because they are predominantly contributed by the N$^\wedge$N ligand. As shown in Fig. 5, **1c** with the significantly lower LUMO energy level and the slightly raised HOMO level has the much smaller HOMO-LUMO energy gap, decreased by 0.49 eV and compared with that of **1a**. While complex **1b** has the opposite trend, the corresponding larger energy gap increases by 0.08 eV with respect to **1a**. For **2b**, the HOMO is significantly increased by 0.19 eV relative to that of **2a** because of the substitution of the pyrrole group by the indole group on the ancillary ligand (N$^\wedge$N) in **2b**, and the LUMO is obviously decreased by 0.33 eV, which may lead to a relatively small HOMO-LUMO energy gap (Fig. 5). For **2c**, the HOMO and LUMO energy levels are calculated to be 0.18 and 0.38 eV lower than **2a**, respectively.

It is also noted that the LUMOs of **1a-2c** are predominantly localized on the N$^\wedge$N moiety with the contribution of about 96%. Furthermore, the energies of HOMO and LUMO are related to the hole- and electron-injection abilities of these complexes. For **2b** and **2c**, the significantly lower LUMO energies will ensure the efficient

electron-injection abilities, while the higher HOMO energies for the complexes **2a** and **2b** will result in the larger hole-injection abilities compared with the others. The different hole-injection abilities and electron-injection abilities will inevitably cause an influence on hole- and electron-injection balance and consequently affect the device performance. We will discuss this aspect in detail in section of performance in OLEDs.

Absorption spectra in CH$_2$Cl$_2$ medium

On the basis of the optimized ground state geometries, the TDDFT/PBE0/6-31G(d) method with PCM in CH$_2$Cl$_2$ medium was performed to calculate the absorption properties of all the studied complexes, and the simulated absorption curves are plotted in Fig. 6. Furthermore, the detailed information, such as the transition energies, oscillator strengths and configurations for the most relevant singlet-singlet and singlet-triplet excited states in each complex are listed in Table S8 together with the experimental results.[18]

In Fig. 6, the absorption spectra of complexes **1a-1c** and **2a-2c** are different in band locations and separations due to the different ancillary ligands. Complexes **1a-1c** have the similar absorption curves in the ultraviolet region between 200-380 nm. Different from **1a** and **1c**, absorption spectra for **1b** show the less intense features at about 389 nm and the tail extending into the visible region. In addition, the spectra of **1a-2c** show strong π-π* peaks in 220-240 nm, and the relatively weak absorption bands (are stronger than those of **2a-2c**) in the range 300-320 nm from **1a-1c**, while the absorption intensity of **2a-2c** shows the intense features in 390-420 nm.

It can be seen that the peak values (274 and 340 nm) calculated with TD-DFT method (Table S8) agree well with the experimental data (around 272 and 324 nm). In addition, the calculated lowest-lying singlet absorptions at 420 nm for **2a** is also in good agreement with the experimental value at 430 nm. In the present calculations, the TD-DFT calculations could, to a certain degree, predict the photophysical behavior of these Ir(III) complexes.

The lowest energy absorption wavelengths follow the order: **2b** (508 nm) > **2c** (487 nm) > **2a** (430 nm) > **1c** (420 nm) > **1a** (361 nm) > **1b** (357 nm) (Table S8), in good agreement with the HOMO-LUMO energy gaps trend (Fig. 5) because the HOMO–LUMO transition configurations are predominantly responsible for the S_0–S_1 transition (**1a**: 95%; **1b**: 97%; **1c**: 92%; **2a**: 91%; **2b**: 96%; **2c**: 98%). From the above analysis on FMOs, the lowest lying absorptions of **1c** and **2c** can be characterized as metal to ligand charge transfer (MLCT) [d(Ir)→π*(N^N)] and ligand to ligand charge transfer (LLCT) [π(C^C)→π*(N^N)], and intraligand charge transfer (ILCT) [π(N^N)→π*(N^N)]. In addition, the character of the lowest-lying absorptions for **1a**, **2a**, and **2b** are predominated by the ancillary ligands and assigned as ILCT[π(N^N)→π*(N^N)]. For **1b**, the transitions can be described as mixed characters of MLCT/LLCT [d(Ir)+π(C^C)→π*(N^N)].

For **1a**, the calculated absorption peaks with the largest oscillator strength is localized at 219 nm, which has the transition configuration of HOMO-4→LUMO+5 described as the [d(Ir)+π(C^C)→π*(C^C)] with the transition characters of MLCT/LLCT/ILCT. For **1b** and **1c**, the transitions with the largest oscillator strengths are located at around 300 and 315 nm, red-shifted about 81 and 96 nm compared with that of **1a**, and have the transition characters of [d(Ir)+π(C^C)→π*(N^N)] /MLCT/LLCT and [d(Ir)+π(C^C+N^N)→π*(N^N)] /MLCT/LLCT/ILCT, respectively. The maximum absorption of complexes **2a-2c** are ascribed to [π(C^C+N^N)→π*(N^N)] /LLCT/ILCT, [π(N^N)→π*(N^N)] /ILCT, and [d(Ir)+π(C^C+N^N)→π*(N^N)] /MLCT/LLCT/ILCT transitions character, and absorptions bands are at 223, 420, and 231 nm contributed by the HOMO-9→LUMO+1(47%), HOMO-2→LUMO(91%), and HOMO→LUMO+4(54%) transition, respectively.

The calculated vertical triplet absorptions of these complexes are at 460, 451, 521, 584, 653, and 553 nm for **1a-2c** (Table S8) with the same transition characters of π(N^N)→π*(N^N)/ILCT except that the **1c** has the vertical triplet absorptions characterized as d(Ir)→π*(N^N) /MLCT, π(C^C)→π*(N^N) /LLCT,

and $\pi(N^\wedge N)\rightarrow\pi^*(N^\wedge N)$ /ILCT characters.

Phosphorescence in CH$_2$Cl$_2$ medium

TDDFT/M062X level in CH$_2$Cl$_2$ medium was used to calculate the phosphorescent spectra of all the studied complexes on the basis of the lowest triplet state geometries. The calculated emission energies, transition nature, and the available experimental values are listed in Table 2. Fig. 7 showed the results together with the available experimental value for **2a**. It can be seen that the B3LYP, PBE0, CAM-B3LYP, and BP86 functionals overestimated emission wavelength compared with the experimental data, especially the BP86 functional with the deviation 78 nm, while the M062X gives satisfactory result for **2a** with smaller discrepancy of 15 nm compared with the experimental data for **2a**.[18] Therefore, we have employed the M062X functional for further emission spectra calculations.

Table 2 shows that the lowest-energy emissions of **1a-2c** mainly originate from the LUMO→HOMO transition assigned to [$\pi^*(N^\wedge N)\rightarrow d(Ir)+\pi(N^\wedge N)$] with the mixed characters of LMCT/ILCT except for **2c**. For **2c**, mixed transitions of LUMO→HOMO-1, and LUMO+1→HOMO are responsible for this emission, which is attributed to the LMCT, LLCT, and ILCT mixed characters (Table 2). These results are consistent with the analysis of the geometry structure of the triplet excited states in the above geometry structure section. The strengthened interactions between the metal and N$^\wedge$N ligand, which was caused by the shortened Ir-ligand bond distances (Ir-N) (Fig. 4), result in the more participation of N$^\wedge$N ligand in the FMOs in the excited states for these studied complexes, while the Ir-C bond lengths show little change and lead to the absence of the C$^\wedge$C ligands in the excited states (Table 2). The remarkable involvement of the LMCT transition in emission for these studied complexes is beneficial to a high quantum yield.

On the other hand, the calculated lowest-energy emissions are at 501 nm (2.47 eV), 504 nm (2.45 eV), 569 nm (2.17 eV), 584 nm (2.12 eV), 707 nm (1.75 eV), and 637 nm (1.94 eV) for **1a-2c**, respectively. In generally, the introduction of electron-withdrawing fluorine substituent has been used not only to modulate the

emission energy but also often to change the ordering of the lowest excited triplet states.[32–34] The peculiarity of fluorine as a substituent lies in the fact that, in addition to the strong inductive effect, its atomic p-orbital has the right energy to interact significantly with the frontier π-orbitals via a mesomeric effect. It is a pity, in this study, comparing complex **1a** with **1b**, the emission wavelength has the slight change from 501 to 504 nm. That is to say, the introduction of fluorine in both heterocycles in complex **1b** is not better than functionalization of the pyridine ring only in complex **1a**. However, the addition of trifluoromethyl substituent in **1c** leads to a stronger stabilization of the LUMO. Indeed, the calculated HOMO-LUMO gap for complex **1c** decreases by 0.49 eV with respect to complex **1a**. Comparing **1a** with **1c**, the emission wavelength has the larger change from 501 to 569 nm, which shows the trifluoromethyl substituent has the strong effect on the electron distribution in complex than the fluorine substituent. In addition, compared with **2a**, the pronounced blue-shifts for **1a** and **1b** have been observed, while the obvious red-shifts were observed for **2b** and **2c**. Therefore, **1a** and **1b** might be potential candidates for blue-emitting phosphorescent materials.

Efficiency comparison

The emission quantum yield (Φ) is linked to the radiative (k_r) and nonradiative (k_{nr}) rate constants, which can be expressed by the following equation, where τ_{em} is the emission decay time:

$$\Phi_{PL} = k_r \tau_{em} = \frac{k_r}{k_r + k_{nr}} \tag{1}$$

Obviously, a large k_r and a small k_{nr} are required to increase the quantum yield. Generally, there are three processes to govern the phosphorescence quantum yields Φ: (1) singlet-triplet intersystem crossing (ISC); (2) radiative decay from a triplet state to the singlet ground state, and (3) nonradiative decay from an excited state to the ground state. If one emitter has fast processes (1) and (2), and slow process (3), it will be a strong emitter.[35]

The k_{nr} from the T_1 to the S_0 states is usually expressed in the form of the energy law equation (2),[36] and the k_r is given by equation (3):[37]

$$k_{nr} \approx \alpha \exp\left(-\beta E_{T_1}\right) \tag{2}$$

$$k_r \approx \gamma \frac{\left\langle \Psi_{S_1} \left| H_{S_0} \right| \Psi_{T_1} \right\rangle^2 \mu_{S_1}^2}{(\Delta E_{S_1-T_1})^2}, \quad \gamma = \frac{16\pi^3 10^6 n^3 E_{T_1}^3}{3h\varepsilon_0} \tag{3}$$

where α, β, and γ are constant. Equation (2) is well-known as "the energy gap law", which indicates that k_{nr} decreases with the increase of the energy of the lowest triplet excited state (E_{T_1}). On the contrary, equation (3) shows that k_r increases with the increase of E_{T_1}. Thus, a large E_{T_1} is essential for an efficient material. Table 3 indicates that **1a** has the largest E_{T_1} followed by **1b** in CH_2Cl_2 medium.

The spin-orbit coupling (SOC) effect is elucidated mainly from the following two aspects. One is the contribution of MLCT in the T_1 state.[38] The direct involvement of the d(Ir) orbital enhances the first-order SOC in the $T_1{\rightarrow}S_0$ transition, which would result in a drastic decrease of the radiative lifetime and avoid the nonradiative process.[39] Thus, a large MLCT contribution facilitates the increase of the quantum yield. Table 3 shows that the contribution of MLCT for **1a-2c** are calculated to be 10.9%, 32.6%, 16.7%, 10.6%, 9.6%, and 16.0%, respectively. The relatively large MLCT contribution is observed in **1b**, **1c** and **2c**. The other aspect elucidating the SOC effect is the S_1-T_1 energy gap ($\Delta E_{S_1-T_1}$).[22] The $S_1{\rightarrow}T_1$ ISC induced by SOC interactions of the triplet state with the singlet state plays an important role in the phosphorescent process. The minimal $\Delta E_{S_1-T_1}$ (S_1-T_1 energy gap) is good for enhancing the transition moment and ISC rate, leading to the increased k_r. Thus, according to equation (3), a large μ_{S_1} and small $\Delta E_{S_1-T_1}$ are also good for a high quantum yield. From Table 3, it can be seen that **1b** has the smallest $\Delta E_{S_1-T_1}$ (0.23 eV) and larger μ_{S_1} (0.45 Debye) among these complexes, forecasting the largest k_r

value. Herein, μ_{S_1} values were obtained in CH_2Cl_2 medium at the PBE0/6-31G(d) functional level. From the above discussion, we can conclude that the assumed complex **1b** should be the most efficient emitting phosphorescent material among these studied complexes.

From the discussion above, the lowest $\Delta E_{S_1 - T_1}$, the largest MLCT contribution, the higher μ_{S_1}, and the larger E_{T_1} values may account for a larger k_r according to equation (3). However, other factors may also play an important role for a high quantum yield, because Φ is the competition between k_r and k_{nr}.

Comparison of performance in OLEDs

To evaluate the energy barrier for the injection of holes and electrons, it is necessary to investigate the ionization potential (IP) and electron affinity (EA), which are also closely related to the HOMO and LUMO, respectively. For photoluminescent materials, a smaller IP value means easier hole injection ability, whereas larger EA value will facilitate electron injection. We also calculated the hole extraction potential (HEP), which is the energy difference between M (neutral molecule) and M^+ (cationic), using M^+ geometry, and electron extraction potential (EEP), which is the energy difference between M and M^- (anionic), using M^- geometry. The calculated vertical IP (IP_v), adiabatic IP (IP_a), vertical EA (EA_v), adiabatic EA (EA_a), HEP, and EEP at the PBE0/6-31G(d) level are listed in Table 4. The IP_v is defined as the energy difference between the cation and its neutral molecule at the equilibrium geometry of the neutral molecule. The IP_a is defined as the energy difference between the cation and its neutral molecule at their own equilibrium geometries. The EA_v is defined as the energy difference between the neutral molecule and its anion both at the equilibrium geometry of the anion.[40] The EA_a is defined as the energy difference between the neutral molecule and its anion at their own equilibrium geometries.

It can be seen that the calculated IP values decrease in the following order: **1b** >

2c > **1c** > **1a** > **2a** > **2b**, indicating the increased hole injection abilities from hole transporting layer to the HOMO of dopants. This order is consistent with the trend of HOMO energies, and thus hole injection for **2a** and **2b** are easier compared with other complexes. Corresponding to the lower LUMO energy levels, the assumed complexes **2a-2c** have the larger EA values and the stronger electron injection ability compared with the complexes **1a-1c**. It is obvious that **2b** exhibits the lowest IP and the higher EA value, indicating that the structure can effectively improve the carrier-injection ability.

According to the Marcus/Hush theory,[41] the rate of intermolecular charge (hole and electron) transfer (k_{et}) can be estimated by the following formula:

$$k_{et} = A \exp\left(-\lambda / 4k_B T\right) \tag{4}$$

where λ is the reorganization energy, A is a prefactor related to the electronic coupling between adjacent molecules, and T and k_B are the temperature and Boltzmann constant, respectively. It has been demonstrated that due to the limited intermolecular charge transfer range in solid state, the mobility of charges dominantly relates to the reorganization energy λ for OLEDs materials.[42,43] Therefore, a low λ value is necessary for an efficient charge transport process.

Herein, λ is determined by the fast change of the molecular geometry when a charge is added or removed from a molecule (the inner reorganization energy λ_i) and slow variations in the surrounding medium due to the polarization effects (the external contribution λ_e). The inner reorganization energy λ_i, and the reorganization energy for hole/electron transfer can be simply defined as follows:

$$\lambda_{ih} = IP_v - HEP \tag{5}$$

$$\lambda_{ie} = EEP - EA_v \tag{6}$$

As shown in Table 4, for most complexes (except **2b**), the reorganization energies for electron transport (λ_e) are slightly larger than the reorganization energies for hole transport (λ_h), which reveals that the hole transport performance of these

complexes are slightly better than the electron transport ability. Table 4 also shows that the introductions of F substitution and the -CF$_3$ group for **1b** and **1c** lead to their relatively higher λ_h and λ_e in comparison with that of **1a**, meaning that they have the poor charge-transporting properties, while **2a-2c** have the opposite trend. The change of the ancillary ligands of complexes **2a-2c** has a significant influence on the reorganization energies, especially for **2b**, in which the λ_h and λ_e are 0.10 and 0.07 eV smaller than those **1a-1c**, respectively (Table 4), resulting in the increased charge-transporting rate for them. Moreover, we also note that the change of the ancillary ligands for **2a-2c** leads to a smaller difference between λ_h and λ_e, demonstrating the improvement of the transfer balance between hole and electron. Especially, the differences between λ_h and λ_e of the assumed complexes **2a** and **2b** are relatively smaller (0.02 and 0.03 eV, respectively), indicating that hole and electron transfer balance could be achieved more easily in the emitting layer, which is the key factor for materials used in OLEDs. Therefore, **2a** and **2b** are more suitable emitters in OLED applications.

Conclusions

In this article, based on the synthesized complex **2a**, we designed five complexes **1a**, **1b**, **1c**, **2b**, and **2c** in order to investigate the influence caused by the introduction of different substituents and the changing ancillary ligands on the optical and electronic properties. The following conclusions can be drawn: (1) For all these complexes (except **2b**), the hole transporting performance is better than the electron-transporting performance, while the change of ancillary ligand for **2b** has an obvious red-shift in optical spectra and the better balance between the hole- and electron-transporting abilities. (2) According to the results, we found that the change of ancillary ligands can stabilize the energy levels of LUMOs more than HOMOs and induce variations in the energy gap between HOMO and LUMO. Thus, the energies and electron distribution of the frontier molecular orbitals (especially the LUMO) can be adjusted through changing the ancillary ligands, which could have a

large influence on the absorption and emission spectra. (3) The detailed analysis on quantum efficiency showed that the assumed **1b** is considered to be a potential candidate of blue-emitting material with high quantum efficiency, due to its relatively larger radiative (k_r) rate and smaller nonradiative (k_nr) rate.

Acknowledgments

Supplementary Information

Table S1 The calculated geometry parameters obtained by different computational methods and basis sets together with the experimental results of complex **2a**. **Tables S2-S7** Frontier molecular orbital energies (eV) and compositions (%) in the ground state for the studied complexes. **Table S8** Selected calculated wavelength (nm)/energies (eV), oscillator strength (*f*), major contribution, transition characters and the experimental wavelength (nm) for **1a-2c** in CH_2Cl_2 medium at TD-PBE0 level.

References

1 J. Kido, K. Hongawa, K. Okuyama and K. Nagai, *Appl. Phys. Lett.* 1994, **64**, 815.

2 A. Tsuboyama, H. Iwawaki, M. Furugori, T. ukaide, J. Kamatani, S. Igawa, T. Moriyama, S. Miura, T. Takiguchi, S. Okada, M. Hoshino and K. Ueno, *J. Am. Chem. Soc.* 2003, **125**, 12971.

3 S. W. Lai and C. M. Che, Luminescent Cyclometalated Diimine Platinum(II) Complexes: Photophysical Studies and Applications, in Transition Metal and Rare Earth Compounds, Springer, Berlin, Heidelberg, 2004.

4 D. M. Han, G. Zhang, H. X. Cai, X. H. Zhang and L. H. Zhao, *J. Lumin.* 2013,

138, 223.

5 M. Mazzeo, V. Vitale, F. Della Sala, M. Anni, G. Barbarella, L. Favaretto, G. Sotgiu, R. Cingolani and G. Gigli, *Adv. Mater*. 2005, **17**, 34.

6 M. A. Baldo, D. F. O'Brien, Y. You, A. Shoustikov, S. Sibley, M. E. Thompson and S. R. Forrest, *Nature*. 1998, **395**, 151.

7 S. Lamansky, P. Djurovich, D. Murphy, F. Abdel-Razzaq, H. -E. Lee, C. Adachi, P. E. Burrows, S. R. Forrest and M. E. Thompson, *J. Am. Chem. Soc*. 2001, **123**, 4304.

8 M. L. Ho, F. M. Hwang, P. N. Chen, Y. H. Hu, Y. M. Cheng, K. S. Chen, G. H. Lee, Y. Chi and P. T. Chou, *Org. Biomol. Chem*. 2006, **4**, 98.

9 M. Schmittel and H. W. Lin, *Inorg. Chem*. 2007, **46**, 9139.

10 Q. Zhao, F. Y. Li, S. J. Liu, M. X. Yu, Z. Q. Liu, T. Yi and C. H. Huang, *Inorg. Chem*. 2008, **47**, 9256.

11 M. A. Baldo, S. Lamansky, P. E. Burrows, M. E. Thompson and S. R. Forrest, *Appl. Phys. Lett.* 1999, **75**,4.

12 R. J. Holmes, S. R. Forrest, Y. J. Tung, R. C. Kwong, J. J. Brown, S. Garon and M. E. Thompson, *Appl. Phys. Lett*. 2003, **82**, 2422.

13 D. M. Han, G. Zhang, T. Li, H. G. Li, H. X. Cai, X. H. Zhang and L. H. Zhao, *Chemical Physics Letters*. 2013, **573**, 29.

14 C. Adachi, M. A. Baldo, S. R. Forrest and M. E. Thompson, *Appl. Phys. Lett*. 2000, **77**, 904.

15 S. Okada, K. Okinaka, H. Iwawaki, M. Furugori, M. Hashimoto, T. Mukaide, J. Kamatani, S. Igawa, A. Tsuboyama, T. Takiguchi and K. Ueno, *Dalton Trans*. 2005, 1583.

16 Y. Y. Lyu, Y. Byun, O. Kwon, E. Han, W. S. Jeon, R. R. Das and K. Char, *J. Phys. Chem. B*. 2006, **110**, 10303.

17 X. H. Shang, D. M. Han, S. Guan and G. Zhang, *J. Phys. Org. Chem*. 2013, **26** 784.

18 K. Y. Lu, H. H. Chou, C. H. Hsieh, Y. H. Yang, H. R. Tsai, H. Y. Tsai, L. C. Hsu, C. Y. Chen, I. C. Chen and C. H. Cheng, *Adv. Mater*. 2011, **23**, 4933.

19 E. Runge and E. K. U. Gross, *Phys. Rev. Lett*. 1984, **52**, 997.

20 A. D. Becke, *J. Chem. Phy*s. 1993, **98**, 5648.

21 C. T. Lee, W. T. Yang and R .G. Parr, *Phys. Rev. B*. 1988, **37**, 785.

22 I. Avilov, P. Minoofar, J. Cornil and L. De Cola, *J. Am. Chem. Soc*. 2007, **129**, 8247.

23 C. Adamo and V. Barone, *J. Chem. Phys*. 1999, **110**, 6158.

24 P. J. Hay and W. R.Wadt, *J. Chem. Phys*. 1985, **82**, 270.

25 T. Helgaker and P. Jørgemsen, *J. Chem. Phys*. 1991, **95**, 2595.

26 E. Cancès, B. Mennucci and J. Tomasi, *J. Chem. Phys*. 1997, **107**, 3032.

27 Y. Zhao and D.G. Truhlar, *Theor. Chem. Acc*. 2008, **120**, 215.

28 J. P. Perdew, *Phys, Re .B*. 1986, **33**, 8822.

29 C. Cramer and D. Truhlar. Solvent Effects and Chemical Reactivity; Kluwer: Dordrecht, The Netherlands, 1996.

30 M. J. Frisch, G. W. Trucks, H. B. Schlegel, G. E. Scuseria, M. A. Robb, J. R. Cheeseman, G. Scalmani, V. Barone, B. Mennucci and G. A. Petersson, et al. Gaussian 09, Revision B.01; Gaussian, Inc., Wallingford CT, 2010.

31 N. M. O′Boyle, A. L. Tenderholt and K. M. Langner, *J. Comput. Chem*. 2008, **29**, 839.

32 A. B. Tamayo, B. D. Alleyne, P. I. Djurovich, S. Lamansky, I. Tsyba, N. N. Ho, R. Bau and M. E. Thompson, *J. Am. Chem. Soc*. 2003, **125**, 7377.

33 S. J. Su, H. Sasabe, T. Takeda and J. Kido, *Chem. Mater*. 2008, **20**, 1691.

34 E. Orselli, R. Q. Albuquerque, P. M. Fransen, P. Froehlich, H. M. Janssen and L. De Cola, *J. Mater. Chem*. 2008, **18**, 4579.

35 G. Tong and C. Che, *Chem. Eur. J*. 2009, **15**, 7225.

36 J. S. Wilson, N. Chawdhury, M. R. A. Al-Mandhary, M. Younus, M. S. Khan, P. R. Raithby, A. Kohler and R. H. Friend, *J. Am. Chem. Soc*. 2001, **123**, 9412.

37 H. Yersin, Highly Efficient OLEDs with Phosphorescent Materials, Wiley-VCH, Weinheim, Germany, 2008.

38 J. Li, P. I. Djurovich, B. D. Alleyne, M. Yousufuddin, N. N. Ho, J. C. Thomas, J. C. Peters, R. Bau and M. E. Thompson, *Inorg. Chem*. 2005, **44**, 1713.

39 C. H. Yang, Y. M. Cheng, Y. Chi, C. J. Hsu, F. C. Fang, K. T. Wong, P. T. Chou, C. H. Chang, M. H. Tsai and C. C. Wu, *Angew. Chem. Int. Ed*. 2007, **46**, 2418.

40 J. C. Rienstra-Kiracofe, G. S. Tschumper, H. F. Schaefer, S. Nandi and G. B. Ellison, *Chem. Rev.* 2002, **102**, 231.

41 R. A. Marcus, *Rev. Mod. Phys*. 1993, **65**, 599.

42 N.S. Hush, *J. Chem. Phys*. 1958, **28**, 962.

43 G. R. Hutchison, M. A. Ratner and T. J. Marks, *J. Am. Chem. Soc*. 2005, **127**, 2339.

Table 1 Main optimized geometry parameters of **1a-2c** in the ground and the lowest lying triplet states at the PBE0/6-31G(d) level

	1a		1b		1c		2a		2b		2c	
	S_0	T_1	S_0	T_1	S_0	T_1	S_0	T_1	S_0	T_1	S_0	T_1
Ir-N1	2.122	2.139	2.132	2.133	2.127	2.147	2.112	2.120	2.140	2.112	2.126	2.116
Ir-N2	2.169	2.160	2.180	2.160	2.176	2.144	2.162	2.143	2.164	2.144	2.173	2.152
Ir-C1	2.031	2.028	2.030	2.029	2.029	2.030	2.031	2.029	2.034	2.033	2.035	2.035
Ir-C2	2.029	2.034	2.029	2.035	2.031	2.037	2.033	2.036	2.034	2.043	2.032	2.036
Ir-C3	2.039	2.034	2.036	2.035	2.039	2.032	2.060	2.038	2.038	2.042	2.038	2.038
Ir-C4	2.031	2.038	2.038	2.039	2.040	2.040	2.033	2.035	2.034	2.035	2.030	2.033
N1-Ir-N2	76.46	76.68	76.67	76.70	76.59	76.38	75.73	76.10	75.44	76.17	75.25	76.32
C1-Ir-C2	78.95	78.94	78.98	78.93	78.91	78.90	78.90	78.92	78.84	78.79	78.94	78.94
C3-Ir-C4	78.94	78.99	79.01	78.93	78.94	78.99	78.94	78.96	78.98	78.75	78.98	79.02
N1-Ir-C1	90.29	89.38	89.33	89.77	89.24	89.02	90.90	90.37	90.41	91.44	89.93	90.02
C1-Ir-C3	95.22	93.66	94.53	93.22	94.45	93.52	94.52	94.31	95.24	92.89	95.06	94.59
N1-Ir-N2-C1	-89.2	-89.5	-89.2	-88.9	-88.0	-89.2	-89.2	-88.4	-88.2	-89.6	-89.6	-88.0
C1-Ir-C2-C3	92.2	92.5	91.5	93.1	92.5	93.4	92.2	94.3	93.8	93.4	91.4	91.0

Table 2 Calculated phosphorescent emission of the studied complex in CH_2Cl_2 medium at the TDDFT/M062X level, together with the experimental value

Complexes	λ(nm)/E(eV)	Major configuration	Character	Exp[a]
1a	501/2.47	L→H(99%)	π*(N$^\wedge$N)→d(Ir)+π(N$^\wedge$N) (LMCT/ILCT)	
1b	504/2.45	L→H(96%)	π*(N$^\wedge$N)→d(Ir)+π(N$^\wedge$N) (LMCT/ILCT)	
1c	569/2.17	L→H(93%)	π*(N$^\wedge$N)→d(Ir)+π(N$^\wedge$N) (LMCT/ILCT)	
2a	584/ 2.12	L→H(96%)	π*(N$^\wedge$N)→d(Ir)+π(N$^\wedge$N) (LMCT/ILCT)	599
2b	707/1.75	L→H(87%)	π*(N$^\wedge$N)→d(Ir)+π(N$^\wedge$N) (LMCT/ILCT)	
2c	637/1.94	L→H-1(28%)	π*(N$^\wedge$N)→d(Ir)+π(C$^\wedge$C) (LMCT/LLCT)	
		L+1→H (29%)	π*(N$^\wedge$N)→d(Ir)+π(N$^\wedge$N) (LMCT/ILCT)	

[a] Data from ref. 18.

Table 3 Computed emitting energy (E_{T_1}, in eV), metal-based charge transfer character (^{3}MLCT) (%) and singlet-triplet splitting energy ($\Delta E_{S_1\text{-}T_n}$, in eV, n = 1, 2, 3), along with the transition dipole moment in the $S_0{\rightarrow}S_1$ transition (μ_{S_1}) (Debye) for the studied complexes in CH_2Cl_2 medium

	E_{T_1}	^{3}MLCT	$\Delta E_{S_1\text{-}T_1}$	$\Delta E_{S_1\text{-}T_2}$	$\Delta E_{S_1\text{-}T_3}$	μ_{S_1}
1a	2.47	10.9	0.95	0.15	0.04	0.13
1b	2.45	32.6	0.23	0.01	-0.07	0.45
1c	2.17	16.7	0.75	0.01	-0.12	0.08
2a	2.12	10.6	0.93	0.02	-0.09	0.27
2b	1.75	9.6	0.69	0.03	-0.35	0.57
2c	1.94	16.0	0.57	0.20	-0.04	0.09

Table 4 The calculated vertical IP (IP_v), adiabatic IP (IP_a), hole extraction potential (HEP), vertical EA (EA_v), adiabatic EA (EA_a), electron extraction potential (EEP), reorganization energies for electron (λ_{ie}) and hole (λ_{ih}), and $\Delta = \mid \lambda_{ih} - \lambda_{ie} \mid$ (in eV) at the PBE0/6-31G(d) level for the studied complexes.

	IP_v	IP_a	HEP	EA_v	EA_a	EEP	λ_{ih}	λ_{ie}	Δ
1a	5.90	5.80	5.72	0.02	0.14	0.30	0.17	0.40	0.23
1b	5.99	5.91	5.81	0.15	0.16	0.25	0.21	0.47	0.26
1c	5.92	5.80	5.80	0.38	0.48	0.51	0.32	0.66	0.34
2a	5.78	5.69	5.61	0.43	0.51	0.30	0.16	0.18	0.02
2b	5.64	5.49	5.33	0.66	0.52	0.64	0.10	0.07	0.03
2c	5.97	5.88	5.67	0.70	0.57	0.72	0.14	0.29	0.15

Figure captions:

Fig. 1 Schematic structures for the studied complexes.

Fig. 2 Calculated bond length variations of complex **2a** compared with the experimental results.

Fig. 3 Optimized structure of **2a** in the ground state.

Fig. 4 Calculated bond length variations between the lowest singlet state and the lowest triplet state for complexes **1a-2c**. (The negative values represent the bond distances contracted in the lowest triplet state, while the positive ones indicate an elongation for the bonds in the T_1 state.)

Fig. 5 Contour plots of the HOMO and LUMO for the studied complexes **1a-2c**.

Fig. 6 Simulated absorption spectra of **1a-2c** in CH_2Cl_2 medium.

Fig. 7 Emission wavelengths for **2a** at M062X, PBE0, B3LYP, CAM-B3LYP, and BP86 levels, respectively, together with the experimental value.

1a	R_1=F	R_2=H
1b	R_1=F	R_2=F
1c	R_1=CF$_3$	R_2=H

2a   2b   2c
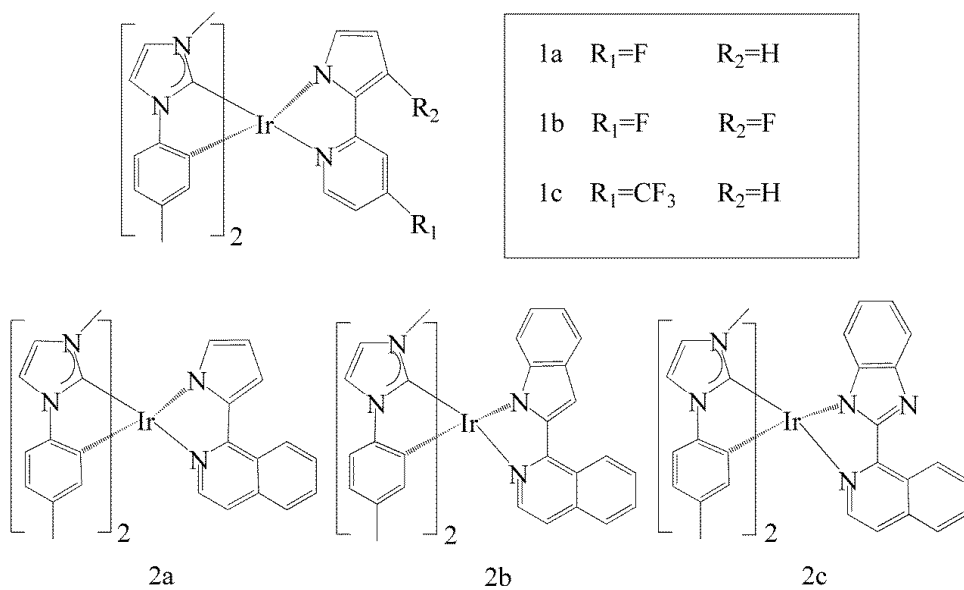
Fig. 1 Schematic structures for the studied complexes.
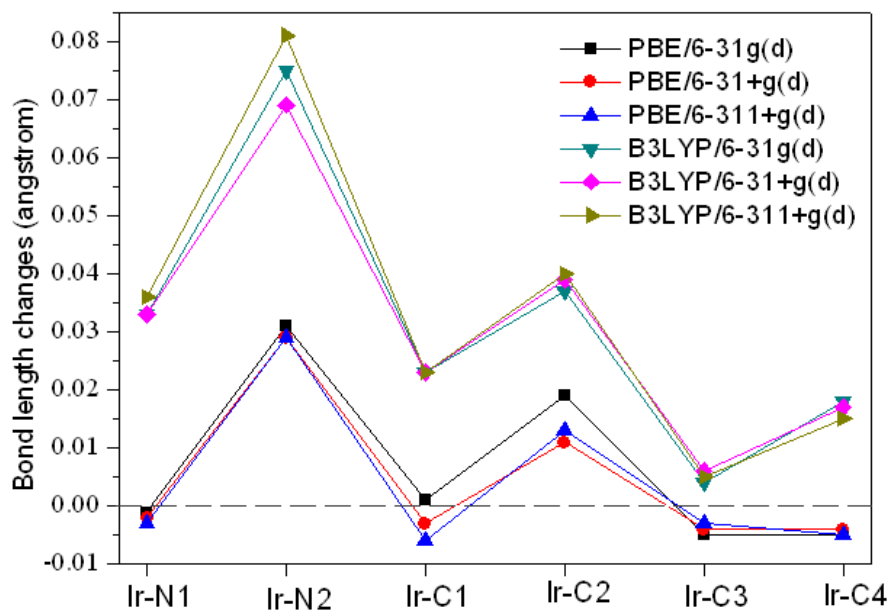
Fig. 2 Calculated bond length variations of complex **2a** compared with the experimental results.
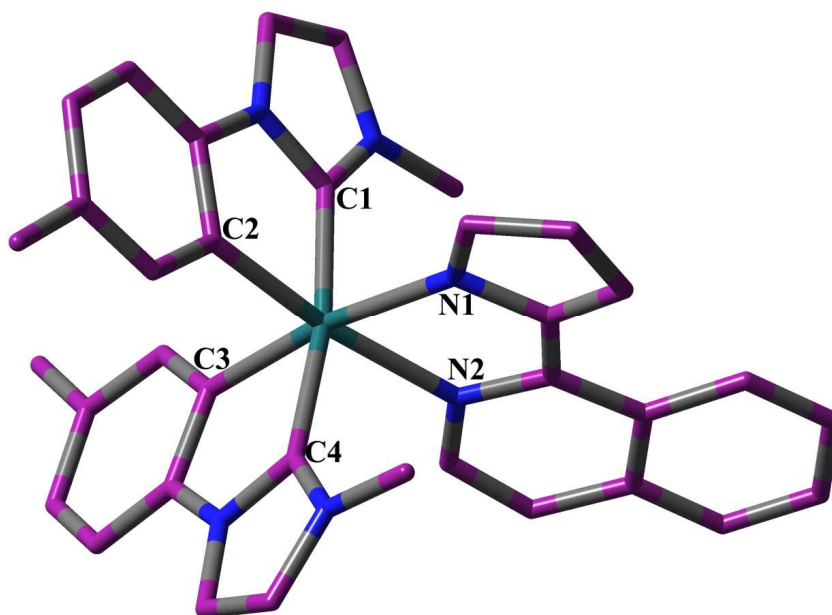
Fig. 3 Optimized structure of **2a** in the ground state at the PBE0/6-31G(d) level .
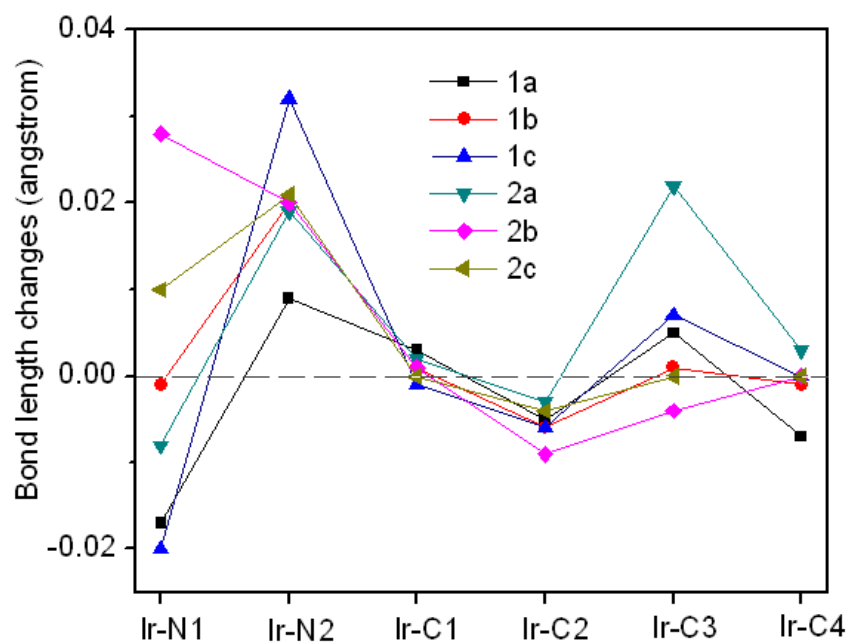
Fig. 4 Calculated bond length variations between the lowest singlet state and the lowest triplet state for complexes **1a-2c** at the PBE0/6-31G(d) level. (The positive values represent the bond distances contracted in the lowest triplet state, while the negative ones indicate an elongation for the bonds in the T_1 state.)
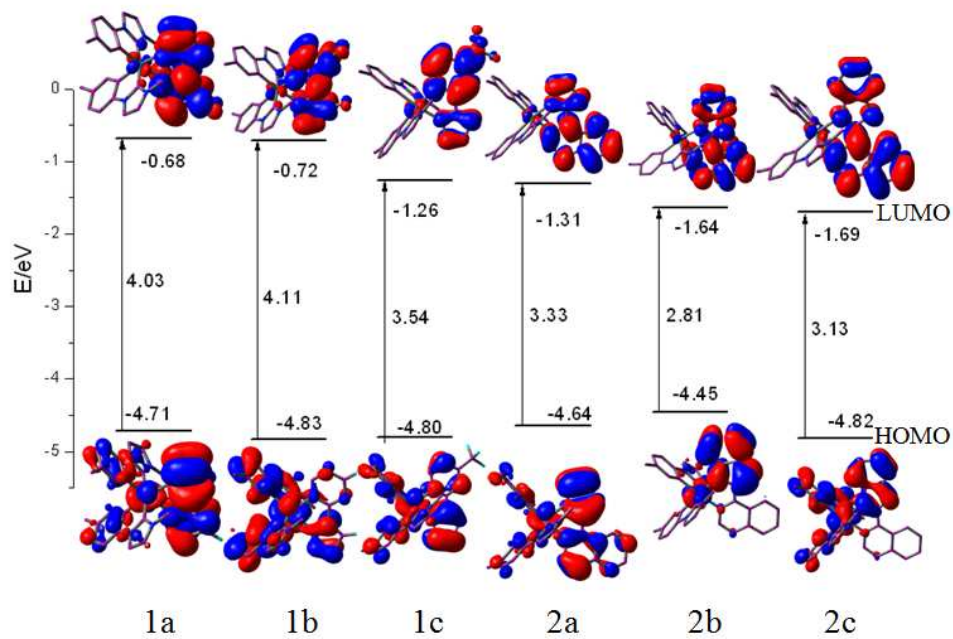
Fig. 5 Contour plots of the HOMO and LUMO for the studied complexes **1a-2c**.
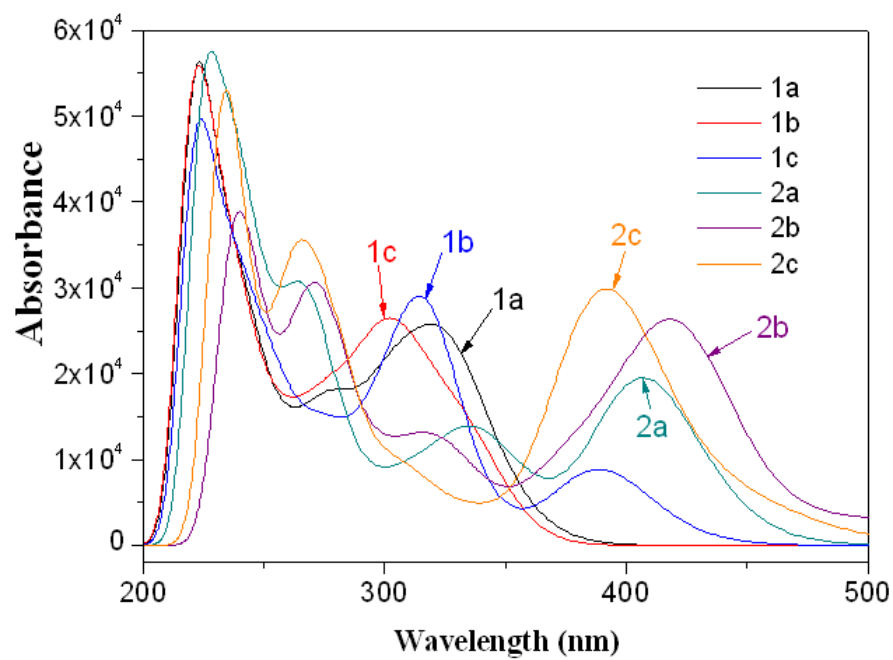
Fig. 6 Simulated absorption spectra of **1a-2c** in CH$_2$Cl$_2$ medium.
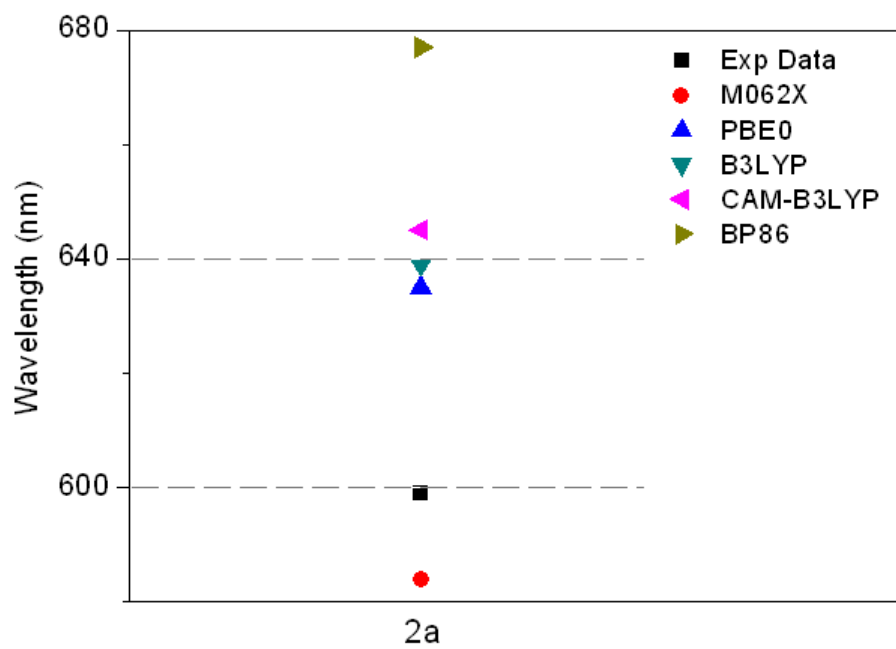
Fig. 7 Emission wavelengths for **2a** at M062X, PBE0, B3LYP, CAM-B3LYP, and BP86 levels, respectively, together with the experimental value.

The theoretical analysis of a series of heteroleptic iridium(III) complexes by using the density functional theory (DFT) method to investigate their electronic structures, photophysical properties, and the phosphorescent efficiency mechanism.